RP Current Trends In Applied Sciences (e-ISSN: 2583-7486)
Vol. 4, No. 1 (January – March 2025) pp. 1–5
DOI:

RESEARCH PLATEAU PUBLISHERS

Cite this article: D. Singh, Synthesis, characterization and spectroscopic measurements of ZnO nanoparticles, *RP Cur. Tr. Appl. Sci*. **4** (2025) 1–5.

Original Research Article

Synthesis, characterization and spectroscopic measurements of ZnO nanoparticles

Devender Singh*

Department of Physics, Government College, Matanhail (Jhajjar) – 124106, Haryana, India
*Corresponding author, E-mail: devender079dudi@gmail.com

ARTICLE HISTORY
Received: 17 Nov. 2024
Revised: 15 Feb. 2025
Accepted: 17 Feb. 2025
Published: 20 Feb. 2025

KEYWORDS
Optical properties;
Chemical synthesis;
Semiconductors;
Nanostructures;
Catalytic properties.

ABSTRACT
Zinc sulfate and sodium hydroxide were used as starting ingredients in a straightforward precipitation method to synthesize zinc oxide nanoparticles. For two hours, the synthesized sample was treated at various temperatures. Energy dispersive spectroscopy (EDS), proton-induced X-ray emission (PIXE) analysis, scanning electron microscopy (SEM), and X-ray diffraction (XRD) were used to analyze the samples. SEM pictures of ZnO synthesized using the aforementioned technique display a variety of morphological changes. Using Debye-Scherrer's formula, the average crystallite sizes of the samples were determined from the whole width at half maximum of XRD peaks and were discovered to be in the nano-range. EDS demonstrates that the aforementioned method yielded extremely pure ZnO nanostructures. The PIXE technique was employed to analyze ZnO's trace elements. Calculations of the optical band gaps of different ZnO powders were made using UV-visible diffuse reflectance spectroscopy.

1. Introduction

Due to its advantageous qualities and potential uses in a variety of fields, including catalysts [1], sensors [2], photoelectron devices [3, 4], and extremely useful and efficient devices [5], nano-sized semiconductor particles have attracted a lot of attention in recent years. These nanomaterials are of great scientific interest in both basic and applied domains due to their unique electrical, structural, and thermal properties. At ambient temperature, the energy gap of zinc oxide (ZnO), a semiconductor with a broad band gap, is 3.37 eV. Because of its photochemical, electrical, optoelectronic, and catalytic qualities, it has been used extensively [6–9]. ZnO nanostructures' strong catalytic activity and vast surface area make them ideal for use in catalytic reaction processes [10]. Since the morphology of nanostructures affects the physical and chemical properties of zinc oxide, it is important to examine not only different synthesis techniques but also the physical and chemical characteristics of generated zinc oxide in relation to its shape. Numerous techniques, including laser ablation [11], hydrothermal methods [12], electrochemical depositions [13], sol–gel method [14], chemical vapor deposition [15], thermal decomposition [16], and combustion method [17, 18], have been documented in the literature for the fabrication of ZnO nanostructures. Ultrasound [19], microwave-assisted combustion [20], two-step mechano-chemical-thermal synthesis [21], anodization [22], co-precipitation [23], and electrophoretic deposition [24] have all been used recently to create ZnO nanoparticles.

By adjusting various precipitation process parameters, including solution concentration, pH, and washing medium, Rodrigues-Paez et al. [25] synthesized ZnO nanoparticles with various morphologies. In this work, a straightforward precipitation technique was used to synthesize ZnO nanostructures. ZnO nanostructures were synthesized using sodium hydroxide and zinc sulfate heptahydrate as precursors. X-ray diffraction (XRD) and scanning electron microscopy (SEM) were used to characterize the prepared samples, while energy dispersive spectroscopy (EDS) and proton-induced X-ray emission (PIXE) studies were used to assess the sample's purity. The samples' band gap energies were determined using diffuse reflectance spectroscopy. The morphology, crystallite dimensions, and optical characteristics of ZnO nanostructures were examined, and an effort was made to associate the optical properties of ZnO with its morphology and crystallite dimensions.

2. Materials and methods

2.1 Materials

The studies employed sodium hydroxide and zinc sulfate heptahydrate. Gracia Enterprises (New Delhi, India) supplied all of the analytical reagent-grade chemicals utilized, and solutions were prepared using deionized water.

Synthesis of ZnO

Zinc sulfate aqueous solution was vigorously stirred for 12 hours while sodium hydroxide solution was added gradually dropwise in a molar ratio of 1:2. After filtering, the resulting precipitate was carefully cleaned with deionized water. Agate mortar was used to grind the precipitate to a fine powder after it had been dried in an oven set at 100°C [26]. The powder produced by the aforementioned process was calcined for two hours at various temperatures, including 300°C, 500°C, 700°C, and 900°C.

2.2 Characterization

XRD and SEM

XRD and SEM were used to characterize the compounds' appearance and structure. A Bruker D_8 Advanced X-ray diffractometer (Bruker Optik GmbH, Ettlingen, Germany) equipped with CuK_α radiation (λ = 1.5418 Å, rated at 1.6 kW) was used to record the XRD patterns of the powdered samples. A Philips XL 30 ESEM scanning electron microscope (FEI-Philips Company, Hillsboro) was used to take SEM pictures of the samples.

UV–vis diffuse reflectance spectroscopy

The optical absorption characteristics of ZnO were characterized using UV-vis spectroscopy. Using $BaSO_4$ as a reference, the samples' UV–vis absorption spectra were captured in the 200–800 nm wavelength range using a Shimadzu UV 3600 UV–vis-NIR spectrometer (Shimadzu Corporation, Kyoto, Japan) in diffuse reflectance mode. At room temperature, spectra were captured, and the Kubelka-Munk function was used to convert the data [27].

Proton-induced X-ray emission

Pure graphite and finely ground samples were combined in a 1:1 ratio (150 mg each), homogenized, and then compressed into a pellet with a diameter of 13 mm. PIXE measurements have been performed on a 3-MV horizontal pelletron accelerator [28]. On the target, the proton beam was collimated to a 3 mm diameter. A Si(Li) detector was maintained at a 90° angle to the direction of the beam. With a beryllium window that is 12 μm thick and an active area of 30 mm^2, the detector offers an energy resolution of 170 eV at 5.9 keV. A current integrator attached to the target holder was used to measure the integrated charge on the sample. Before entering the Si(Li) detector, the X-rays exiting the chamber through a 95-μm Mylar window passed through a 4 cm air gap.

The targets were maintained at a 45° angle to the beam in the PIXE chamber. The beam current was maintained between 3 and 10 nA, and the Si(Li) detector was positioned 90° from the beam. A Canberra MCA [29] (Canberra Industries, Meriden, CT, USA) was used to record the spectra, which were then moved to a personal computer [30].

GUPIX-95 [31], a program that offers nonlinear least-square spectrum fitting, was used to perform PIXE spectral analysis. Since the target was sufficiently thick to completely stop the proton beam, the thick-target PIXE investigation was carried out. Using the macrometer standards and other approved reference materials, an external standard technique was used to verify the chosen analysis process and input parameters. The values were then normalized in accordance with this.

3. Results and discussion

Catalyst characterization

XRD analysis

Figure 1 displays the XRD patterns of the ZnO powders made using the aforementioned technique and calcined at various temperatures. The hexagonal ZnO wurtzite structure is well-indexed to all of the diffraction peaks (JCPDS no. 36–1451). The great purity of the synthesized products was confirmed by the absence of diffraction peaks associated with the contaminant in the XRD patterns. As the calcination temperature rises, the peak intensity rises as well, suggesting greater crystallinity. The produced materials are in the nanoscale range, as indicated by a distinct line broadening of the diffraction peaks at 300°C, 500°C, and 700°C. Using the whole width at half maximum of 100, 002, and 101 of the X-ray diffraction peaks, Debye-Scherrer's equation (Equation 1) computed the average crystallite sizes of the samples, as shown in Table 1 [32].

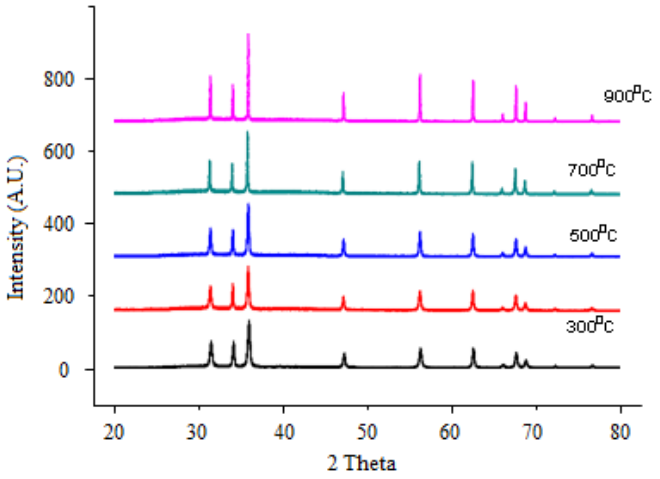

Figure 1: XRD patterns ZnO nanoparticles after calcination at various temperatures.

Table 1: Average ZnO crystallite size as determined by XRD with Equation (1)

Calcination temperature (°C)	Crystallite size, D (nm)
300	64
500	74
700	131
900	187

As the calcination temperature rises, the average crystallite size also rises. The sample that was calcined at 900°C shows a notable increase in crystallite size. Grain boundaries migrate at such high temperatures, resulting in the coalescence of small grains and the creation of big grains.

$$D = \frac{0.89\lambda}{\beta \cos\theta} \quad (1)$$

where λ is the incident X-ray wavelength (nm), β is the full width at half maximum, θ is the diffraction angle, and D is the crystallite size (nm).

SEM and EDS analysis

Figure 2 displays the samples' SEM pictures. The temperature at which ZnO is calcined alters its morphologies. When the samples are calcined at 700°C, they transform from nanoflakes that were formed at 300°C and 500°C. The SEM pictures of ZnO samples demonstrate how much less particle aggregation occurs with this preparation technique. Nanoparticles are visible in high-resolution SEM pictures of ZnO that has been calcined at 300°C and 500°C (Figure 2b). It is evident from the energy dispersive spectra of the samples derived from the SEM-EDS analysis (Figure 3) that the sample made using the aforementioned method contains pure ZnO phases.

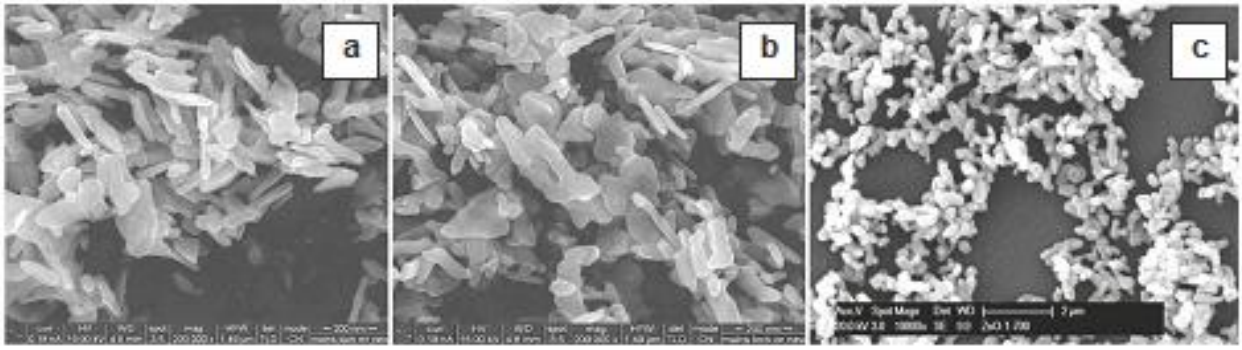

Figure 2: SEM pictures of ZnO samples that were calcined at three distinct temperatures: (a) 300°C, (b) 500°C, and (c) 700°C.

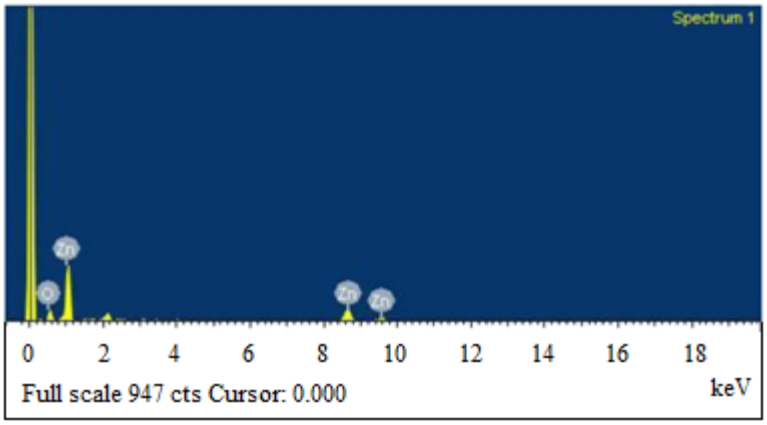

Figure 3: EDS of ZnO calcined at 500°C.

Diffuse reflectance analysis

Figure 4 displays the samples' UV-visible absorption spectra. Below 400 nm, all of the samples exhibit a significant absorption maximum. Samples calcined at 500°C and 700°C exhibit a change in absorption maxima toward higher wavelengths. The agglomerations in the samples are responsible for this red shift [33]. Figure 5 illustrates how the linear part of the graph between the modified Kubelka-Munk function $[F(R)h\nu]^2$ vs photon energy ($h\nu$) is extrapolated to get the band gap energy of the samples [27]. It is challenging to determine the band gap of the 900°C-calcined samples due to their low reflectance. As the calcination temperature rises, ZnO's band gap decreases. This is because ZnO's particle size increases as the calcination temperature rises. Table 2 displays the band gaps of the samples.

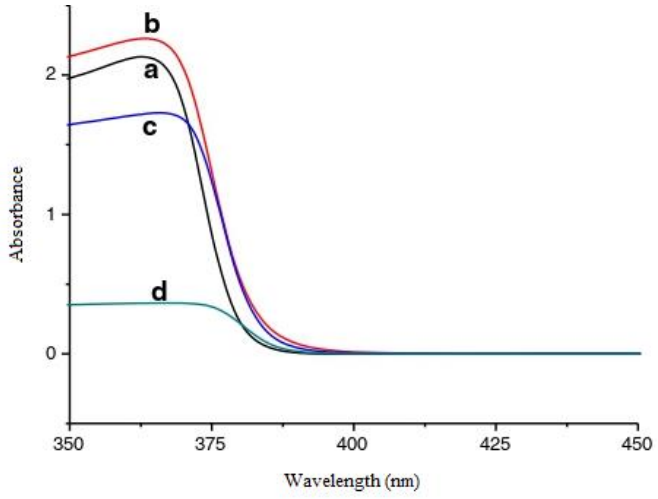

Figure 4: UV–vis absorption spectra of ZnO samples that were calcined at: (a) 300°C, (b) 500°C, (c) 700°C, and (d) 900°C.

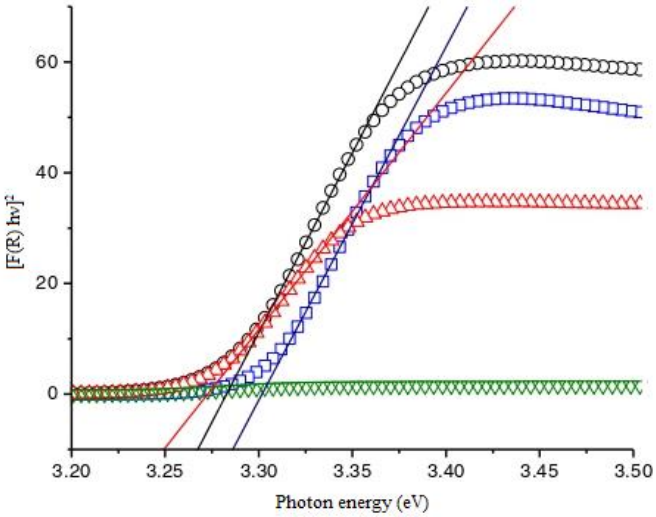

Figure 5: Plots showing the Kubelka-Munk function against energy for ZnO calcined at different temperatures.

Table 2: The optical band gap of various ZnO samples that were calcined at varying temperatures

Calcination temperature (°C)	Bandgap (eV)
300	3.30
500	3.28
700	3.27

Table 3: Elemental concentrations in ZnO nanoparticles

Element	Concentration	Statistical error (%)
Ti	1000 ppm	10
Fe	900 ppm	12
Zn	99.75%	0.2

PIXE analysis

GUPIX software is used to examine the samples in order to determine the trace elements and purity of the ZnO nanoparticles. The synthesized ZnO nanoparticles have 99.8% purity, with trace levels of impurities including Fe and Ti, according to the results displayed in Table 3. The dominating characteristic peak of Zn is reflected in the PIXE spectrum of the ZnO nanoparticle that was calcined at 300°C (Figure 6). However, because the minimum detection limit of the corresponding elements has increased, the pile-up continuum may comprise the distinctive X-ray lines of trace impurities like Pb that are not visible in the spectra and cannot be quantified. Regarding the limit of detection of contaminants at the trace level, the significance of efficiently suppressing the pile-up continuum is evident. The limits of detection for trace elements are worse because the pile-up continuum of significant elements, as zinc in this instance, may overlap the X-ray lines of trace elements. However, if these specific elements are present, their concentration must be substantially lower because the residual concentration is only a few thousand parts per million, which may not have a major impact on the materials' purity. Thus, the PIXE analysis validates the efficiency of our method for preparing nanoparticles.

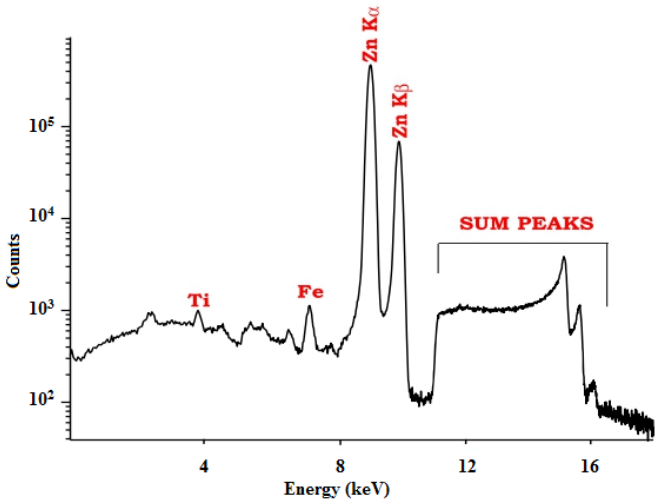

Figure 6: PIXE spectrum of 300°C-calcined ZnO.

4. Conclusions

A straightforward precipitation technique was used to synthesize ZnO nanoparticles. The XRD and EDS measurements unequivocally show that the aforementioned process produces extremely pure ZnO. ZnO SEM photos demonstrate how the calcination temperature altered the morphology. The produced material's excellent purity and trace levels of elements like Fe and Ti were verified by PIXE analysis. An increase in calcination temperature reduced the band gap of ZnO and pushed the absorption maximum to higher wavelengths.

Acknowledgements

The author is very much debited to Dr. S. Duhan, Deenbandhu Chhotu Ram University of Science and Technology, Murthal, India, for providing instrumental facility to carry out the XRD, SEM and PIXE analyses.

Authors' contributions

The author read and approved the final manuscript.

Conflicts of interest

The author declares no conflict of interest.

Funding

This research received no external funding.

Data availability

No new data were created.

References

[1] S.S. Joshi, P.R. Patil, M.S. Naimase, P.P. Bakare, Role of ligands in the formation, phase stabilization, structural and magnetic properties of α-Fe_2O_3 nanoparticles, *J. Nanopart. Res*. **5** (2006) 635–643.

[2] X.L. Cheng, H. Zhao, L.H. Huo, S. Gao, J.G. Zhao, ZnO nanoparticulate thin film: preparation, characterization and gas-sensing properties, *Sens. Actuators B* **102** (2004) 248–252.

[3] S.Y. Lee, E.S. Shim, H.S. Kang, S.S. Pang, Fabrication of ZnO thin film diode using laser annealing, *Thin Solid Films* **437** (2005) 31–34.

[4] Z.L. Wang, X.Y. Kong, Y. Ding, P. Gao, W.L. Hughes, Semiconducting and piezoelectric oxide nanostructures induced by polar surfaces, *Adv. Funct. Mater*. **14** (2004) 943–956.

[5] Y.H. Huang, Y. Zang, L. Liu, S.S. Fan, Y. Wei, J. He, Controlled synthesis and field emission properties of ZnO nanostructures with different morphologies, *J. Nanosci. Nanotechnol*. **6** (2006) 787–790.

[6] D. Brida, E. Fortunato, I. Ferreira, H. Aguas, R. Martins, New insights on large area flexible position sensitive detectors, *J. Non-Cryst. Solids* **299** (2002) 1272–1276.

[7] Z.L. Wang, Zinc oxide nanostructures: growth properties and applications, *J. Phys. Condens. Matter*. **16** (2004) R829–R858.

[8] M. Suchea, S. Christoulakis, K. Moschovis, N. Katsarakis, G. Kiriakidis, ZnO transparent thin films for gas sensor applications, *Thin Solid Films* **515** (2006) 551–554.

[9] A. Ashour, M.A. Kaid, N.Z. El-Syed, A.A. Ibrahim, Physical properties of ZnO thin films deposited by spray pyrolysis technique, *Appl. Surf. Sci*. **252** (2006) 7844–7848.

[10] J.C. Chen, C.T. Tang, Preparation and application of granular ZnO/Al_2O_3 catalyst for the removal of hazardous trichloroethylene, *J. Hazard. Mater*. **142** (2007) 88–96.

[11] N. Scarisoreanu, D.G. Metai, G. Dinescu, G. Epurescu, C. Ghica, L.C. Nistor, M. Dinescu, Properties of ZnO thin films prepared by radio-frequency plasma beam assisted laser ablation, *Appl. Surf. Sci*. **247** (2005) 518–525.

[12] Y.H. Ni, X.W. Wei, J.M. Hong, Y. Ye, Hydrothermal synthesis and optical properties of ZnO nanorods, *Mater. Sci. Eng. B, Solid State Mater. Adv. Technol.* **121** (2005) 42–47.

[13] S. Chang, S.O. Yoon, H.J. Park, A. Sakai, Luminescence properties of Zn nanowires prepared by electrochemical etching, *Mater. Lett*. **53** (2002) 432–436.

[14] M. Ristiac, S. Musiac, M. Ivanda, S. Popoviac, Sol–gel synthesis and characterization of nanocrystalline ZnO powders, *J. Alloys Compd*. **397** (2005) L1–L4.

[15] J.J. Wu, S.C. Liu, Low-temperature growth of well-aligned ZnO nanorods by chemical vapor deposition, *Adv. Mater*. **14** (2002) 215–218.

[16] R.C. Wang, C.C. Tsai, Efficient synthesis of ZnO nanoparticles, nanowalls, and nanowires by thermal decomposition of zinc acetate at a low temperature, *Appl. Phys. A*. **94** (2009) 241–245.

[17] D.G. Lamas, G.E. Lascalea, N.E. Walsoc, Synthesis and characterization of nanocrystalline powders for partially stabilized zirconia ceramics, *J. Eur. Ceram. Soc*. **18** (1998) 1217–1221.

[18] S. Badhuri, S.B. Badhuri, Enhanced low temperature toughness of Al_2O_3-ZrO_2 nano/nano composites, *Nanostrct. Mater*. **8** (1997) 755–763.
[19] Z. Khorsand, A. Abid, W.H. Majid, H.Z. Wang, R. Yousefi, M. Golsheikh, Z.F. Ren, Sonochemical synthesis of hierarchical ZnO nanostructures, *Ultrasonic Sonochemistry* **20** (2013) 395–400.
[20] M. Kooti, A. Nagdhi Sedish, Microwave-assisted combustion synthesis of ZnO nanoparticles, *J. Chem*. (2013).
[21] D. Rajesh, B. Vara Lakshmi, C.S. Sunandana, Two-step synthesis and characterization of ZnO nanoparticles, *Physica B-Cond. Mater*. **407** (2012) 4537–4539.
[22] A. Shetty, K. Nanda, Synthesis of zinc oxide porous structures by anodisation with water as an electrolyte, *Appl. Phys. A.* **109** (2012) 151–157.
[23] O. Singh, N. Kohli, R.C. Singh, Precursor controlled morphology of zinc oxide and its sensing behavior, *Sens. Actuators B.* **178** (2013) 149–154.
[24] A. Vazquez, I.A. Lopez, I. Gomez, Growth mechanism of one-dimensional zinc sulfide nanostructures through electrophoretic deposition, *J. Mater. Sci*. **48** (2013) 2701–2704.
[25] J. Rodrigues-Paez, A.C. Caballero, M. Villegas, C. Moure, P. Duran, J.F. Fernandz, Controlled precipitation methods: formation mechanism of ZnO nanoparticles, *J. Eur. Ceram. Soc*. **21** (2001) 925–930.
[26] N. Daneshvar, S. Aber, M.S. Sayed Dorraji, A.R. Khataee, M.H. Rasoulifard, Preparation and investigation of photocatalytic properties of ZnO nanocrystals: effect of operational parameters and kinetic study, *Int. J. Chem. Biom. Eng*. **1** (2008) 24–29.
[27] S. Cimitan, S. Albonetti, L. Forni, F. Peri, D. Lazzari, Solvothermal synthesis and properties control of doped ZnO nanoparticles, *J. Colloid. Interface Sci*. **329** (2009) 73–80.
[28] V. Vijayan, V.S. Ramamurthy, S.N. Behera, S. Puri, J.S. Shanti, N. Singh, Elemental composition of fly ash from a coal fired thermal power plant: a study using PIXE and EDXRF, *X-ray Spectrometry* **26** (1997) 65–68.
[29] V. Vijayan, P.K. Nayak, V. Chakrovortty, Proton induced X-ray emission studies on Indian copper coins, *Ind. J. Phys. A.* **76** (2002) 477–479.
[30] J.A. Maxwell, W.J. Teesdale, J.L. Campbell, The Guelph PIXE software package II, *Nucl. Instrum. Methods B* **95** (1995) 407–421.
[31] H. Gleiter, Nanocrystalline materials, *Prog. Mater. Sci*. **33** (1989) 223–315.
[32] C.C. Chen, P. Liu, C.H. Lu, Synthesis and characterization of nano-sized ZnO powders by direct precipitation method, *Chem. Eng. J.* **144** (2008) 509–513.
[33] B. Babita, D. Kishore Kumar, S.V. Manorama, Hydrothermal synthesis of highly crystalline ZnO nanoparticles: a competitive sensor for LPG and EtOH, *Sens. Actuators B* **119** (2006) 676–682.